Geophysical Journal International

Geophys. J. Int. (2013) **195,** 854–869
Advance Access publication 2013 August 30

doi: 10.1093/gji/ggt313

Self-constrained inversion of potential fields

V. Paoletti,[1] S. Ialongo,[1] G. Florio,[1] M. Fedi[1] and F. Cella[2]

[1] *Dipartimento di Scienze della Terra, dell'Ambiente e delle Risorse, Università 'Federico II' di Napoli, Italy. E-mail: paoletti@unina.it*
[2] *Dipartimento di Scienze della Terra, Università della Calabria, Italy*

Accepted 2013 August 2. Received 2013 July 29; in original form 2013 March 8

SUMMARY

We present a potential-field-constrained inversion procedure based on *a priori* information derived exclusively from the analysis of the gravity and magnetic data (self-constrained inversion). The procedure is designed to be applied to underdetermined problems and involves scenarios where the source distribution can be assumed to be of simple character. To set up effective constraints, we first estimate through the analysis of the gravity or magnetic field some or all of the following source parameters: the source depth-to-the-top, the structural index, the horizontal position of the source body edges and their dip. The second step is incorporating the information related to these constraints in the objective function as depth and spatial weighting functions. We show, through 2-D and 3-D synthetic and real data examples, that potential field-based constraints, for example, structural index, source boundaries and others, are usually enough to obtain substantial improvement in the density and magnetization models.

Key words: Inverse theory; Gravity anomalies and Earth structure; Geopotential theory; Magnetic anomalies: modelling and interpretation; Magnetic field.

1 INTRODUCTION

One of the main difficulties in potential field inversion is obtaining satisfactory depth-to-source resolution from measured data. This happens because inverse potential field problems are ill-posed, and therefore inherently difficult to solve. Specifically, they may not have a unique solution, and the solution may be extremely sensitive to errors. As described below, these difficulties are due to certain kinds of ambiguities such as the inherent, algebraic and error ambiguity (Fedi *et al.* 2005). All of these kinds of ambiguity may lead to a loss of depth information and add to the problem of obtaining reliable information about the source distribution.

Under the continuous formulation, the unknowns of the inverse problems are functions and not a few parameters. Therefore, the solution contains an infinite number of variables and the inverse problem is highly underdetermined and ill-posed. For magnetic problems, the inverse problem can be mathematically described as a Fredholm integral equation of the first kind:

$$\int_{\Omega} K(\mathbf{r}, \mathbf{r}_0) f(\mathbf{r})\, d\mathbf{r}^3 = T(\mathbf{r}_0). \tag{1}$$

Here, $\mathbf{r} \in \Omega$ is a point inside the source volume Ω and $\mathbf{r}_0$ denotes an observation point outside Ω. The function K is Green's function for the gravitational or magnetic sources.

As is well known, the inverse potential field problem in the form of (1) has inherently ambiguous solutions, due to Green's third identity: if one allows the domain Ω to be infinite, then any field T outside Ω can be produced by both a source distribution inside Ω and an infinitely thin layer of sources at the surface of Ω. This represents the physical basis of the non-uniqueness of the potential field inverse problem. To overcome the ambiguity problem in the continuous formulation (1) one must incorporate *a priori* information regarding the causative physical property distribution in suitable regularization algorithms (e.g. Fedi *et al.* 2005). Thus, the role of regularization is to avoid non-uniqueness and instability (e.g. Hansen 1998).

In order to solve the potential field problem with real data, we must discretize the continuous problem and represent the solution f by a finite amount of information. This introduces some *a priori* information by the definition of the source volume Ω and its discretization in a 3-D grid of rectangular blocks of known size, in which the unknown source magnetization is piecewise constant. This leads to a system of linear equations:

$$\mathbf{Am} = \mathbf{b}, \tag{2}$$

where the right-hand side $\mathbf{b}$ consists of the measured data that we can consider as noisy samples of the continuous field T. The solution vector $\mathbf{m}$ consists of the values of the piecewise continuous solution in each cell. Finally, the coefficient matrix $\mathbf{A}$ has elements given by

$$\mathbf{A}_{ij} = \int_{\Omega_j} K(\mathbf{r}, \mathbf{r}_{0,i})\, d\mathbf{r}^3, \tag{3}$$

where Ω_j denotes the jth cell and $r_{0,i}$ is the ith data point. The matrix **A** has dimensions $M \times P$ where M is the number of measurements and P is the number of cells.

Any discretization of a linear inverse problem (1) has a regularizing effect on the solution. In fact, the effect of the discretization can be considered as a restriction of the infinite-dimensional problem onto a finite-dimensional one (Engl *et al.* 1996). However, in most applications, the coefficient matrix **A** will have a very large condition number, meaning that the discrete solution **m** is very sensitive to perturbations. Hence, in any application with noisy data, the discretization does not provide enough stabilization to allow the computation of a useful solution. Data noise, as well as model errors and rounding errors, are amplified by the large condition number, and call for additional stabilization in order to filter these contributions to the solution.

Furthermore, whenever we face a linear system of the form (2), we encounter an algebraic ambiguity when the system is underdetermined, that is, when $M < P$ (less data than unknowns). In this situation, the matrix has a non-trivial null space, and any component of the solution in this null space cannot be determined. One possibility is to compute the minimum-norm solution, that is, the model **m** whose 2-norm is minimum; it is unique because the null-space component is zero. However, in practice, these minimum-norm solutions may not be useful. In fact, because of the inverse law versus distance characterizing potential fields, one minimizes the 2-norm of **m** by using shallow sources with low source density (or magnetization), and thus the minimum-norm solutions are very shallow. Square or overdetermined systems usually lack algebraic ambiguity and the (least squares) solution is, in principle, algebraically unique. In practice, rounding errors often prevent us from computing a unique solution and noise can make the unique (least squares) solution useless. All these difficulties call for additional *a priori* information to overcome the consequent ambiguity.

A simple approach to reduce ambiguity is to deal with overdetermined problems by using a parametric discretization, in which the solution consists of basic geometric body shapes with homogeneous density/magnetization distributions (e.g. Corbato 1965; Cordell & Henderson 1968; Al-Chalabi 1971; McGrath & Hood 1973; Whitehill 1973; Pedersen 1977). When the possible solutions to the problem are simple-shaped and contained in a region of limited extent, ambiguity is considerably reduced.

When dealing with a non-parametric approach and with underdetermined problems, several other kinds of *a priori* information—besides the mentioned division of source volume into elementary homogeneous cells of known size but unknown density/magnetization—may be used in the objective function formulation. When compactness is required, one can use a compactness criterion to let the causative body to be minimum (Last & Kubik 1983), employ a focusing criterion (Portniaguine & Zhdanov 2002), use the Cauchy norm on model parameters to enforce sparseness and depth-weighting of the solution (Pilkington 2009). Some authors (Boulanger & Chouteau 2001) combined more constraints, such as minimum distance, flatness and compactness. Other approaches involve a stochastic inversion of gravity/magnetic anomalies that makes use of: a parameter covariance matrix estimated from physical property data (Chasseriau & Chouteau 2003), probability density functions to perform a lithologic inversion (Guillen *et al.* 2008), borehole and surface data to limit the resulting solution space (Shamsipour *et al.* 2012). A 2-D method for inverting potential field data with model constraints designed by the interpreter was presented by Silva & Barbosa (2004). The authors also presented an adaptive learning procedure for incorporating prior knowledge (Silva & Barbosa 2006). Wijns & Kowalczyk (2007) proposed a semi-automatic procedure that allows the interpreter to set a geologically reasonable solution. With the aim of incorporating depth information and regularizing the solution, Barnes & Barraud (2012) developed an inversion algorithm that solves for the geometric interface between geological bodies.

Other relevant ways to introduce *a priori* information involve constraints somewhat limiting the variation range of some parameters, such as positivity for density and magnetization or constraints for upper and lower density bounds (Li & Oldenburg 1996; Portniaguine & Zhdanov 2002). Other types of constraints may be used to force the solution to match with some predefined source characteristics, given by empirical laws or external information from drill logs, geological studies and other geophysical investigations. Refer to Silva *et al.* (2001) and Silva & Barbosa (2004) for an exhaustive description of types of constraints in inversion.

The lack of depth resolution in underdetermined discrete problems led Li & Oldenburg (1996, 1998) to introduce a depth-weighting function in the Tikhonov formulation that counteracts the natural decay of the kernel functions (whose parameters depend on the discretization). Their model objective function can also incorporate *a priori* information through spatial weighting functions that enhance or attenuate the structural complexity in different regions/directions. Ash *et al.* (2006), Farquharson *et al.* (2008) and Williams *et al.* (2009) followed this approach to constrain gravity and/or magnetic inversion by incorporating information derived from drill log data in the model objective function. Lelièvre & Oldenburg (2009) showed that incorporating orientation information into underdetermined potential field inversions can improve the results and yield a better depth resolution.

Such procedures lead to a reduction of the general ambiguity. But they usually rely on relatively strong assumptions based on information from other than potential fields about the source characteristics, which may be too subjective.

As regards the depth-weighting, Cella & Fedi (2012) studied simple sources, such as spheres, cylinders, dykes and contacts, and showed that the depth-weighting exponent should be associated not to the field decay of a single cell (as in Li & Oldenburg 1996, 1998), but to the structural index, a parameter related to the source type. The important point is that this parameter may be either assumed or determined by a direct estimate on the field itself. This choice gives substantial objectivity to the depth-weighting function and to the consequent solutions.

Besides inversion, other methods such as multiscale boundary analysis (Fedi & Florio 2001; Fedi 2002) and *Depth from Extreme Points* (*DEXP*) method (Fedi 2007) can yield effective information about the field sources in terms of lateral extent, depth and source type, as shown in Cella *et al.* (2009) and Paoletti *et al.* (2007, 2013).

Following the above approach, we may try to take advantage of different kinds of information (structural index, source horizontal boundaries and depth) which are typically extracted by potential field practitioners, but that are usually managed separately, in order to build a reasonable model. More specifically, we want to implement this kind of information—self-extracted from potential field—directly in the inversion algorithm, with the aim of obtaining reliable inversion solutions for underdetermined problems. In this sense, we will distinguish between external (deriving from drill logs and, geological and geophysical information e.g. Paoletti *et al.* 2012; Rapolla *et al.* 2012; Secomandi *et al.* 2013) and

potential-field-based constraints, such as the structural index and the position and dip of the source edges. Obviously, both kinds of constraints, if available, are important to get a reliable inverse model, but we are here interested specifically in verifying whether the introduction of the sole potential-field-based constraints is useful to produce valid source models.

We note that whereas in the case of very simple density or magnetization distributions, a 2-D modelling may already yield good results, in the case of more complex property distributions, a constrained inversion may point out the presence of density/magnetization variations within the body source and show possible irregularities in the bounds' patterns and positions.

2 SELF-CONSTRAINTS

Here, we briefly describe the different types of constraints which are typically retrieved from potential field data analysis: (1) the structural index N, which may be estimated through well-known methods such as *Euler Deconvolution* (e.g. Barbosa *et al.* 1999; Nabighian & Hansen 2001) or through multiscale methods such as the *Multiridge Euler Deconvolution* (e.g. Florio & Fedi 2006; Fedi *et al.* 2009; Florio & Fedi 2013) and *Scaling Function Method* (e.g. Florio *et al.* 2009); (2) the depth-to-the-top or to the centre of the source, as estimated by methods such as the CWT (e.g. Sailhac *et al.* 2000), *Multiridge Geometric Method* (Fedi *et al.* 2009), the *DEXP Method* (Fedi 2007) and/or the above cited *Multiridge Euler Deconvolution* and *Scaling Function Method*; (3) the position of the source edges, which may be estimated through the computation of the horizontal gradient (Cordell & Grauch 1985) and/or by the *Enhanced Horizontal Derivative* method (Fedi & Florio 2001) or normalized derivatives (e.g. Miller & Singh 1994; Verduzco *et al.* 2004; Wijns *et al.* 2005; Cooper & Cowan 2006); (4) the dip of the edges of the source, inferred by methods such as the cited *Multiridge Geometric Method* and the method proposed by McGrath (1991).

Euler Deconvolution is used to retrieve information about source positions and depths. This method can also be used as a multiscale technique by analyzing the data along potential field ridges, which are lines defined by the position of the extreme points of the field at different scales. Euler equations are notably simplified along any of these ridges (Fedi *et al.* 2009). Since a given anomaly may generate one or more ridges, *Euler Deconvolution* may be used to jointly invert the data along all them, so performing a *Multiridge Euler Deconvolution* (Florio & Fedi 2013). Along with this method, the *Geometric Method* is built by joining extreme points of the analysed field at different altitudes and uses a geometric criterion to find the structural index and vertical and horizontal source positions (Moreau *et al.* 1999; Fedi *et al.* 2009).

The *Scaling Function Method* is a multiscale method based on the study of the scaling function of potential fields. It also allows retrieving source parameters such as depth and structural index through an analysis along ridges. The *DEXP Method* leads to estimates of source depths and density/magnetization from the extreme points of a 3-D field scaled following specific power laws of the altitude; depths to the sources are obtained from the position of the extreme points of the scaled field, and the excess mass or dipole moment are obtained from the scaled field values. Such methods are based on the homogeneous field theory, involving simple sources. For complex sources, the estimated values of the source parameters must be treated as approximate; a more general theory for complex sources and inhomogeneous fields has been developed, as shown in Fedi *et al.* (2012).

The position of the maxima of the *Enhanced Horizontal Derivative* signal—obtained by the computation of the horizontal derivative of a weighted sum of vertical derivatives of increasing order—can effectively detect the location of the edges of sources of different extent and depth (e.g. Bruno *et al.* 2002). Regarding the dip, the method proposed by McGrath (1991) allows a qualitative estimation of the dip of the source edges by evaluating the location of the maxima position of the first horizontal derivative computed at different altitudes. As the horizontal position of the maximum at each altitude does not change only over vertical boundaries, the presence of dipping edges can be easily detected. The methods employing horizontal derivatives require the presence of boundaries that can be approximated as single, near-vertical, sharp boundaries. When the boundaries are not represented by a vertical contact or when several boundaries are close together, the location of the gradient maximum can be offset from the boundary (Grauch & Cordell 1987). The amount of this offset is influenced by the depth of the top edge of the boundary below the observation and by the dip of the boundary.

The mentioned multiscale methods enjoy a good stability due to the inherent properties of the upward continuation process. Moreover, despite of the loss of resolution implied by upward continuation, these methods have a high-resolution power. This is because they work on data transformed through a smoothing-enhancing operator (e.g. Fedi *et al.* 2009), combining in an optimal way the upward continuation and a nth-order differentiation operators. This composite filter, when properly tuned, has a response similar to a bandpass filter, removing both high wavenumber noise and regional fields. Therefore, a search for the best continuation altitudes and differentiation orders by looking at the ridges' shape on a vertical section of the transformed field precedes the application of multiscale methods. The correct altitude range may be easily chosen by excluding the lowest altitudes, at which a low S/N ratio may occur due to the differentiation process, and numerous ridges extending only to a small number of scales are observed. The optimum differentiation order may be chosen by considering that ridges of a homogeneous field generated by an isolated source are straight lines (Fedi *et al.* 2009). Thus, the differentiation order can be increased until the interference is sufficiently low that the ridges tend to be linear.

Following Cella & Fedi (2012), the structural index N determines the exponent β of a depth-weighting function introduced in the regularization matrix $\mathbf{W}_m$ by Li & Oldenburg (1996), which is able to give depth resolution to the model by counteracting the natural decay of the kernel:

$$w(z) = \frac{1}{(z + z_0)^{\beta}}, \tag{4}$$

where z is the depth of layers of the 3-D model and the value of z_0 depends upon the observation height and cell size. The exponent of the depth-weighting function β is, in fact, associated to the fall-off rate of field, and thus to the structural index N (Cella & Fedi 2012). Using N as the exponent of the depth-weighting function allows a good estimation of the source depth and gives substantial objectivity to the form of the depth-weighting function and to the consequent solutions. For simplicity, we will express all the structural index values as in the magnetic case, with N_{MAG} varying from 0 to 3, even when estimated starting from other field types.

In the Tikhonov formulation, the objective function can be written as

$$\phi = \|\mathbf{W}_d(\mathbf{Am} - \mathbf{b})\|^2 + \lambda^2 \|\mathbf{W}_m(\mathbf{m} - \mathbf{m}_0)\|^2 , \quad (5)$$

where $\|\mathbf{W}_d(\mathbf{Am} - \mathbf{b})\|^2$ is the weighted misfit functional ($\mathbf{b}$ are the observed data and $\mathbf{W}_d$ is the inverse covariance matrix) and λ^2 is the trade-off or regularization parameter. The term $\|\mathbf{W}_m(\mathbf{m} - \mathbf{m}_0)\|^2$ is referred to as *model objective function* $\phi_m(m)$ and is the weighted minimum-norm solution with respect to a reference model $\mathbf{m}_0$, which consists of the best estimate of the arithmetic mean physical property value in each cell of the model. The model objective function allows adding several types of constraints in the weighting matrix $\mathbf{W}_m$, such as density/magnetization spatial gradients, and can be explicated as (Li & Oldenburg 1996, 1998; Lelièvre & Oldenburg 2009):

$$\begin{aligned}\phi_m(m) = {} & \alpha_s \int_V w_s w^2(z)(m - m_0)^2 dv \\ & + \alpha_x \int_V w_x w^2(z) \left\{ \frac{\partial(m - m_0)}{\partial x} \right\}^2 dv \\ & + \alpha_y \int_V w_y w^2(z) \left\{ \frac{\partial(m - m_0)}{\partial y} \right\}^2 dv \\ & + \alpha_z \int_V w_z w^2(z) \left\{ \frac{\partial(m - m_0)}{\partial z} \right\}^2 dv, \end{aligned} \quad (6)$$

where w_s, w_x, w_y and w_z are the weights indicating the relative importance of smallness and smoothness thorough the model; α_s, α_x, α_y and α_z are global smallness and smoothness weights and w(z) is the depth-weighting function defined in eq. (4).

The discrete representation of eq. (6) is

$$\begin{aligned}\phi_m(\mathbf{m}) &= (\mathbf{m} - \mathbf{m}_0)^T \left(\mathbf{W}_s^T \mathbf{W}_s + \mathbf{W}_x^T \mathbf{W}_x + \mathbf{W}_y^T \mathbf{W}_y + \mathbf{W}_z^T \mathbf{W}_z \right) \\ &\quad \times (\mathbf{m} - \mathbf{m}_0) \\ &= (\mathbf{m} - \mathbf{m}_0)^T \left(\mathbf{W}_m^T \mathbf{W}_m \right) (\mathbf{m} - \mathbf{m}_0) \\ &= \|\mathbf{W}_m (\mathbf{m} - \mathbf{m}_0)\|^2 . \end{aligned} \quad (7)$$

Each component matrix can be written as the product of three individual matrices and one coefficient, that is (Li & Oldenburg 1996)

$$\mathbf{W}_i = \alpha_i \mathbf{S}_i \mathbf{D}_i \mathbf{Z} \qquad i = s, x, y, z, \quad (8)$$

where $\mathbf{S}_i$ are the diagonal matrices whose elements, given by $\sqrt{w_i}$, represent the spatially dependent 3-D weighting functions. They are defined over each cell for $\mathbf{S}_s$ and over each interface between adjacent cells in the respective directions for $\mathbf{S}_x$, $\mathbf{S}_y$ and $\mathbf{S}_z$. $\mathbf{D}_i$ are the finite-difference operators for each component (with $\mathbf{D}_s$ being the identity matrix and $\mathbf{D}_x$, $\mathbf{D}_y$ and $\mathbf{D}_z$ the matrices representing the finite difference operator along the three spatial directions), $\mathbf{Z}$ is a diagonal matrix that represents the discretized form of the depth-weighting function w(z).

Available geological information may be translated into the model objective function incorporating reference model, bounds and smallness and smoothness weights. The smallness weights (w_s in eq. 6 and $\mathbf{S}_s$ in eq. 8) specify the reliability of the reference model $\mathbf{m}_0$ in each cell. The directional smoothness weights (w_x, w_y and w_z in eq. 6 and $\mathbf{S}_x$, $\mathbf{S}_y$ and $\mathbf{S}_z$ in eq. 8) provide a powerful means of enforcing the solution to vary only within a region of the modelling volume. This will allow obtaining solutions well constrained with respect to the depth-to-the-top and horizontal variations of the source-density distribution.

Further information about the magnetization/density upper bound, according to geological studies of the area, and/or to other geophysical investigations and drill logs, may be added.

3 SYNTHETIC EXAMPLES

To illustrate and prove the utility of our inversion strategy, we present some gravity and magnetic 2-D and 3-D synthetic examples. We show how the solution changes by varying the constraints and explore the dependency of the solution on the depth-weighting exponent β. We employed the same inversion framework as Li & Oldenburg (1996), involving the depth-weighting w(z) and the spatial weighting functions w_x, w_y and w_z. We did not use the reference model $\mathbf{m}_0$ to implement constraints. A positivity constraint was set for all the inversions. Positivity constraints help in stabilizing the solutions and avoiding non-realistic positive/negative density oscillations.

3.1 Vertical fault test

The first test regards the analysis, along a profile, of the gravity field generated by a 2-D vertical step located at $x_0 = 6000$ m, having its top at 300 m depth and a 2700 m thickness (Fig. 1), and with a 1 g cm^{-3} density contrast. The source volume is discretized by 200 × 50 cubic cells with 100 m side. Data spacing is 100 m.

As a first step of our inversion strategy, we evaluated the 2-D source parameters from the analysis of its gravity field. The *Multiridge Euler Deconvolution* (Fedi *et al.* 2009) (Fig. 2a) allowed the estimation of the source *structural index N* and edge locations along the x and z directions (Figs 2b, c and d). The results of the analysis, referring to a third-order differentiation of the field at low continuation altitudes, showed average values of $N_{\mathrm{MAG}} = 0.15$, $x_0 = 5943$ m and $z_0 = 340$ m. The highlighted depth to the top was confirmed by the *DEXP Method* (Fedi 2007) (Fig. 2f). Finally, applying McGrath's method (1991) clearly showed that the fault is vertical (Fig. 2e). We note that a first estimation of the x_0 location and of the edge dip could already be made by the horizontal derivative computed in Fig. 1(a), which showed a x_0 value of 6000 m and the presence of a vertical contact. The analyses shown in Figs 2(d) and (e) confirmed the actual x_0 position and the verticality of the fault, with only a negligible shift with respect to the actual x_0.

The found $N = 0.15$, which will be used to correctly set up the exponent β of the depth-weighting function in the inversions tests (Cella & Fedi 2012), is very low and characteristic of a contact. The corresponding depth will be relative to the top of the structure. However, at very high altitudes, the structure could be seen as a sill, whose N is equal to 1, and in this case, the depth found by inversion will be close to the centre of the structure. Therefore, in our inversions tests (Fig. 3), we used both $\beta = N = 0.15$ to better image the top of the structure (see reconstructions in Figs 3b, c and d), and $\beta = N = 1$ to have an image of the density distribution more balanced around the structure midpoint (see reconstructions in Figs 3e, f and g). The inversions were stopped when the normalized misfit $\|\mathbf{b}_{\mathrm{predicted}} - \mathbf{b}_{\mathrm{observed}}\|_2 / \|\mathbf{b}_{\mathrm{observed}}\|_2$ decreased under the threshold of 1e−11.

The reconstruction obtained without any of the cited constraints, that is, the minimum-norm solution, has no depth resolution, even though it gives some information about the lateral position of the fault (Fig. 3a). The solution model obtained by using as a constraint only the depth-weighting function with the exponent $\beta = 0.15$ (Fig. 3b) shows a maximum density distribution located at the

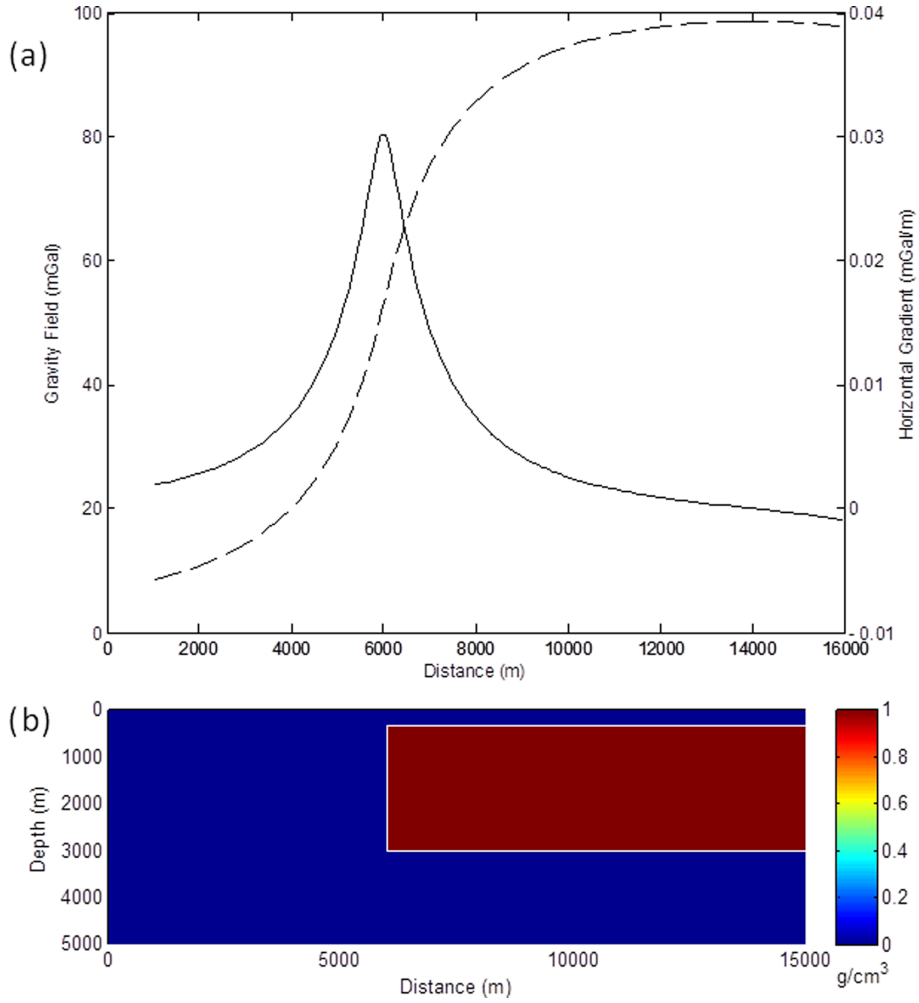

Figure 1. (a) Gravity anomaly generated by a vertical fault model with 1 g cm^{-3} density, 300 m depth-to-the-top and 2700 m thickness (dashed line) and modulus of the horizontal gradient of the gravity anomaly (solid line). (b) Synthetic fault model.

correct depth-to-the-top, due to the correct estimation of N performed by the *Multiridge Euler Deconvolution* (Figs 2b and c). We note, however, that the recovered reconstruction is blurred and provides no clear information about the source top and horizontal boundaries. So, according to our procedure, we repeated the inversion by adding a further constraint about the horizontal position of the source edge and about the edge dip (Fig. 3c). The results of the analyses shown in Figs 1(a) and 2(d) and (e) let us set up the constrained inversion so that an abrupt horizontal density change was favoured to occur at $x_0 = 6000$ m, and at any depth. At this stage, we did not yet input information about the source depth, other than that based on N. A last constraint about the depth-to-the-top was finally added in the reconstruction shown in Fig. 3(d). The constraint was set up at a depth of 300 m, equal to the thickness of three cubic cells. The inclusion of this last constraint lead to a more focused solution, with both the top and horizontal edge clearly detected. The density distribution is still not uniform, but close to the real value (1 g cm^{-3}).

Similar conclusions may be drawn when using $\beta = N = 1$, which allows obtaining a density distribution more balanced around the structure midpoint (see reconstructions in Figs 3e, f and g). The edge and dip-constrained solutions obtained using $\beta = 0.15$ and $\beta = 1$ are actually rather similar, with a better reconstruction in the deeper part of the source when using $\beta = 1$, as should be expected. This led us to an important conclusion: when adding constraints other than the only depth-weighting (such as edge position, depth-to-the-top and dip), the choice of the value of depth-weighting is not more decisive in correctly shaping the source distribution.

In order to show this point, we repeated the inversion, resorting to values of the depth-weighting function that are commonly used for three-dimensional problems and not allowed in a two-dimensional case, such as the value 2 advocated for by Li & Oldenburg (1998) for the gravity inversion, and the value 3 normally used for the magnetic cases (Li & Oldenburg 1996). In Fig. 4, we show the reconstructions obtained employing these two values of β and then adding the same constraints as used in Fig. 3. We note that whereas the reconstructed maximum densities obtained by setting the depth-weighting functions as retrieved by our data analysis (Figs 3b–g) are all very close to the real maximum value of 1 g cm^{-3} and only slightly overestimated in a few cases, the maximum densities obtained by using $\beta = 2$ and $\beta = 3$ are constantly overestimated, especially when inversions are constrained only by the depth-weighting function. This is because the higher the β values, the deeper are the resulting source distributions. This leads to an increase of the density values versus β. The inclusion of constraints other than the only depth-weighting (Figs 4b, c, e and f) reduces this density overestimation, confirming that the choice of weighting used

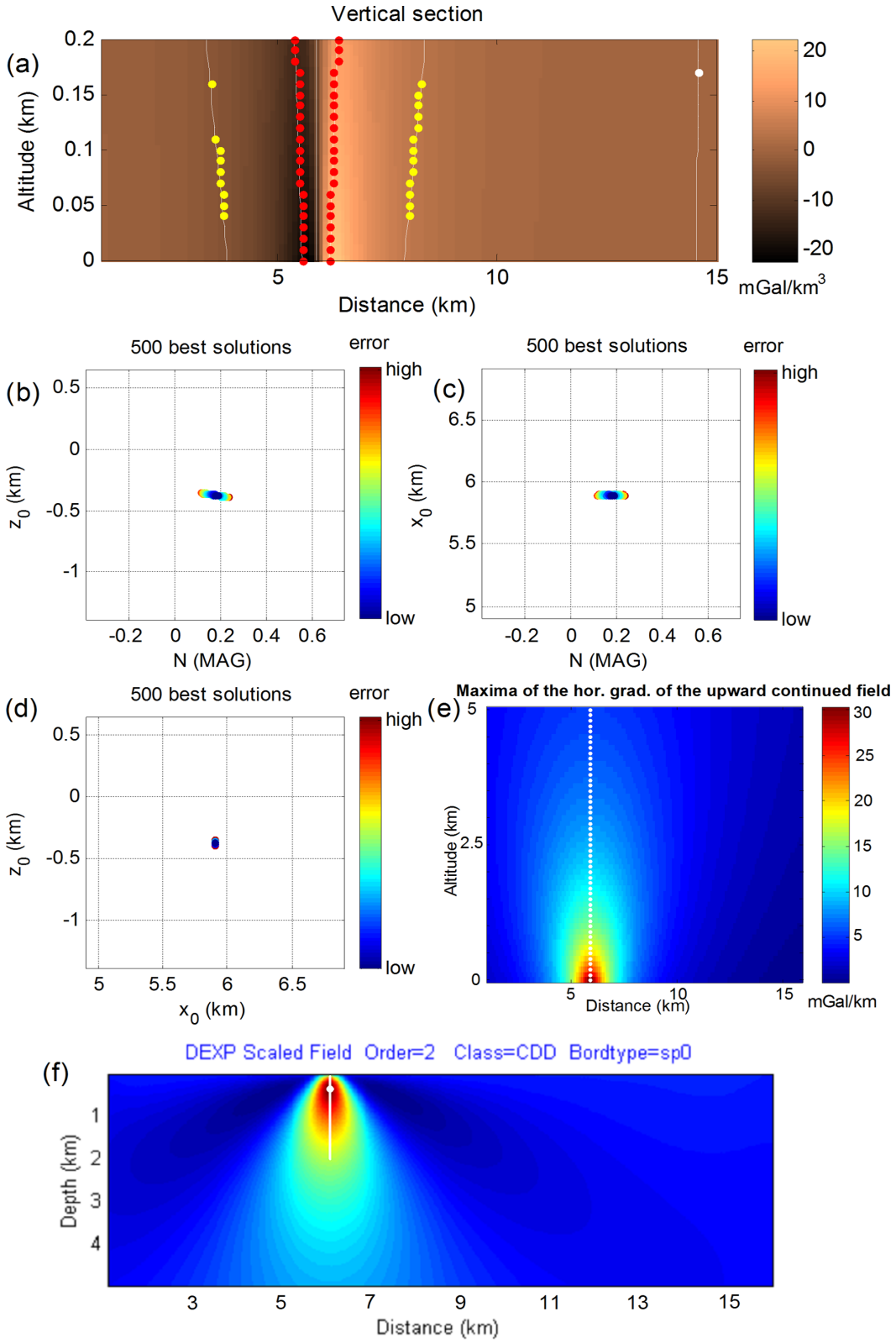

Figure 2. Analysis of the vertical fault data shown in Fig. 1(a). (a)–(d) Results of the *Multiridge Euler Deconvolution* applied to the third-order differentiation of the field at low altitudes giving information about the source N, x_0 and z_0. (e) Plot of maxima of the horizontal gradient of the upward continued field showing that the fault is vertical. (f) *DEXP* analysis yielding information about the source z_0 and confirming that the fault is vertical (Fedi & Pilkington 2012).

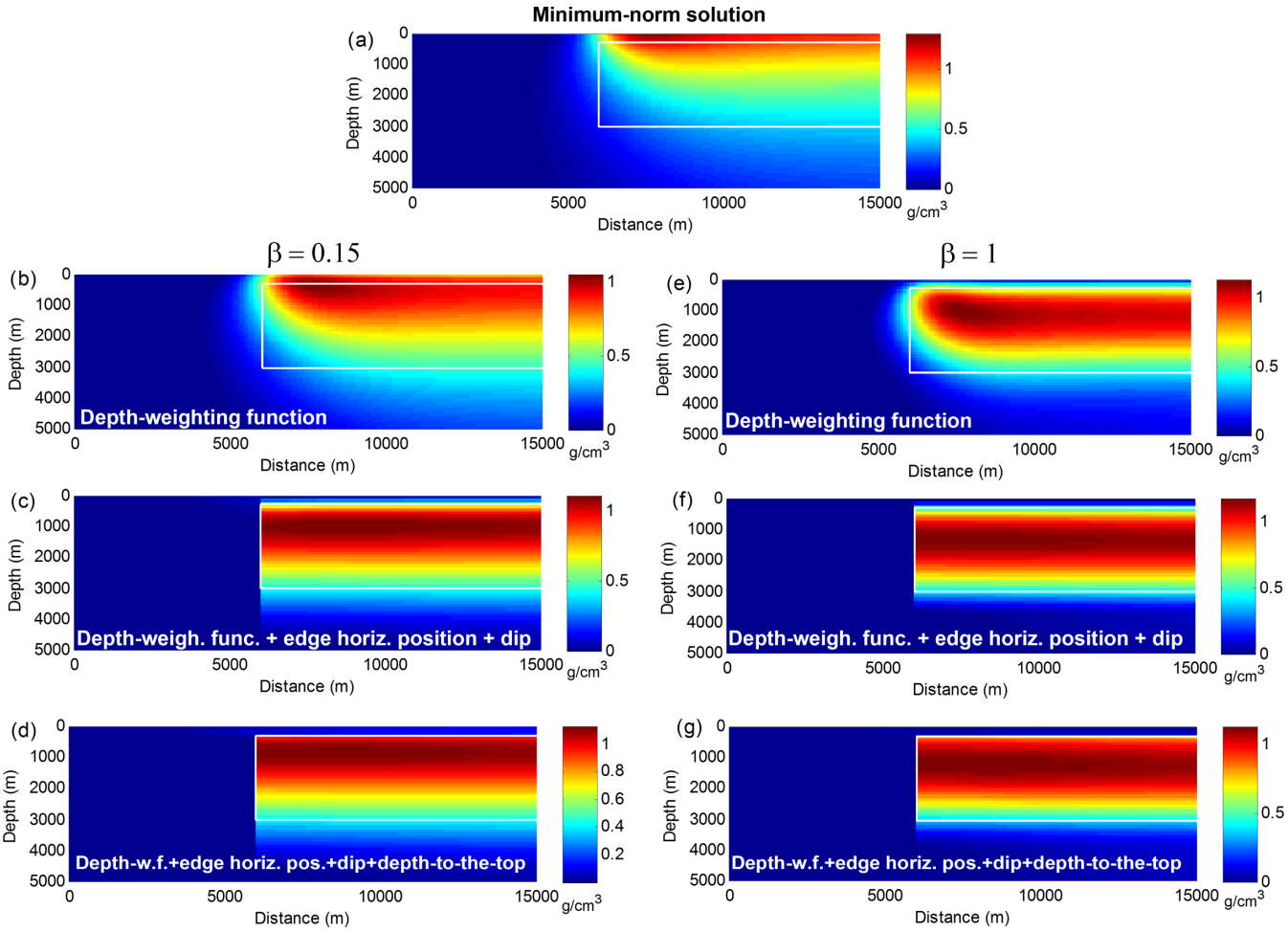

Figure 3. Density models obtained from the inversion of the vertical fault data in Fig. 1(a) by resorting to different self-constraints. (a) Reconstruction obtained without any self-constraint. This solution has no depth resolution, even though it gives information about the lateral location of the fault. (b) Density solution constrained by using a depth-weighting function with $\beta = N = 0.15$ retrieved from the data analysis (see Fig. 2b). The source top is reconstructed at its correct depth, but the recovered density distribution is blurred. (c) Solution with the additional constraint coming from the edge horizontal location and from the dip evaluation (see Figs 2d and e, respectively): the reconstruction is well constrained with respect to source edge and dip. (d) Solution with a further constraint on the location of the source depth-to-the-top (see Figs 2d and f): the solution is now more focused, with both the top and horizontal edge clearly detected. (e)–(g) Same as plots (b)–(d) but with $\beta = N = 1$, which allows obtaining a density distribution more balanced around the structure midpoint. In all the panels, the lines outline the actual source position.

becomes less crucial in correctly characterizing the source property distribution.

3.2 Dipping fault test

The second test regards the analysis, along a profile, of the gravity field generated by a 2-D dipping fault with an inclination of 45°, whose upper edge is located at $x_0 = 6000$ m. The step has its top at 300 m depth, a thickness of 2700 m (Fig. 5b) and a density contrast of 1 g cm^{-3}. The source volume discretization and data spacing are the same as for the vertical fault test.

In order to test the effectiveness of our approach, even in the presence of small to moderate data perturbations, we ran the inversions adding to the data a Gaussian noise with zero mean and standard deviation of 0.25 mGal (Fig. 5a).

We followed the same strategy carried out for the previous test, first evaluating the 2-D source parameters from the analysis of its noisy gravity field.

The *Scaling Function* analysis (Florio *et al.* 2009), carried out through the computation of the sixth-order vertical derivative of the horizontal gradient of the gravity field (Fig. 6a), yielded information about the sources' depth-to-the-top and structural index N (Fig. 6b), showing values of $N_{\mathrm{MAG}} = 0.1$ and $z_0 = 350$ m. The highlighted depth-to-the-top was confirmed by the *DEXP Method* (Fedi 2007; Fig. 6d). The *DEXP* section also shows an asymmetry of the scaled field with respect to a vertical line, consistent with the source dip and interpretable as a qualitative estimate of the source dip. Applying McGrath's method (1991) clearly showed that the fault is dipping towards the East (Fig. 6c). The *Multiridge Geometric Method* (Fedi *et al.* 2009) was applied to the third- and first-order vertical derivatives to obtain two estimates of the source position, relative to different points along the sloping boundary (Figs 6e and f). These estimates were used to calculate the dip of the sloping boundary. The dip turned out to be about 46°, which is in agreement with the true dip of 45°.

Similarly to what was done for the vertical fault, the parameters estimated from the analysis of the gravity field of the dipping fault

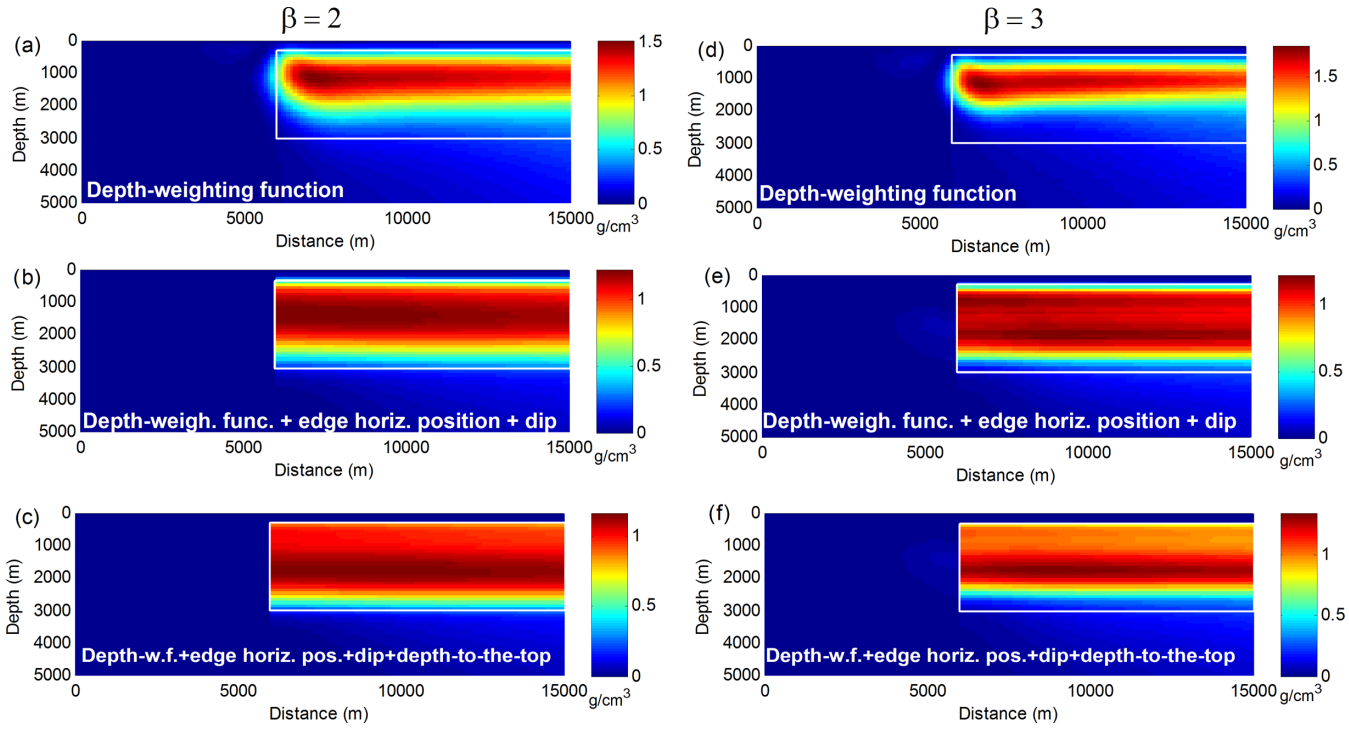

Figure 4. Density models obtained from the inversion of the vertical fault data in Fig. 1(a) by using the same self-constraints as in Fig. 3 and by resorting to values of the depth-weighting function commonly used for three-dimensional problems, such as the value 2 (used for gravity problems) and the value 3 (used for magnetic cases, Li & Oldenburg 1996, 1998). Different from Fig. 3, the maximum densities are here constantly overestimated, especially when inversions are constrained only by the depth-weighting function. The inclusion of constraints other than the only depth-weighting (plots b, c, e, and f) reduces this density overestimation, confirming that the choice of weighting used becomes less crucial in correctly characterizing the source properties when constrains are used.

were used to constrain the inversion tests (Fig. 7), which were stopped when the normalized misfit decreased under the threshold of 1e−05. We used again both the indices $N = 0.1$ and $N = 1$ to better image the top of the structure (Figs 7b, c and d), and the midpoint of the fault, respectively (Figs 7e, f and g). The constraint about the depth-to-the-top retrieved by the application of the *Scaling Function* analysis (Figs 6a and b) was set up again at a depth of 300 m, equal to the thickness of three cubic cells. The constraint about the horizontal position of the source edge was added by imposing a strong lateral density variation at any depth and at the horizontal positions defined by the dipping surface found by the *Multiridge Geometric method* (Figs 6e and f).

We note that the presence of noise in the data did not affect the quality of the solutions (Fig. 7), which are comparable to those obtained for the vertical fault, with a better uniformity of the density distribution for the reconstructions of the dipping fault constrained with respect to the edges and dip of the source. The solutions obtained by using $\beta = 0.1$ and $\beta = 1$ and adding the edge and dip constraints are very similar and this leads us to conclude again that the introduction of other constraints makes the information relative to depth-weighting not crucial for correctly reconstructing the source features.

3.3 Two bodies source

The third test involves the magnetic field (Fig. 8a) generated by two 3-D prismatic sources, which are located rather close to each other, with a location for the shallow source at x: 2200–2700 m, y: 1400–2000 m, z: 150–450 m and for the deep source x: 2100–2800 m, y: 2500–3300 m, z: 450–850 m (Fig. 8c). The source volume is discretized by 50 × 50 × 25 cells, with a 100 m × 100 m × 50 m side. Data spacing is 100 m and we set an inclination of 60° and declination of 0° for both the inducing field and the source magnetization vector.

The location of the source edges was inferred by the computation of the *Enhanced Horizontal Derivative* signal (Fedi & Florio 2001; Fig. 8b). The EHD signal was composed by using the field, the first and the second vertical derivatives and unit weights. The maxima of the EHD signal picked out the actual position of the edges of the two sources, except for a slight shift due to reciprocal interference of the signals, in correspondence with one edge of the deeper source along the y-axis. The *Scaling Function* analysis (Florio *et al.* 2009), carried out for both sources (Figs 9a and b) through the computation of the third-order vertical derivative of the total field, yielded information about the sources' depth and structural index N. For the shallow source, we retrieved z_0: 250 m and $N_{\mathrm{MAG}} = 2.2$, while for the deep source we found z_0: 690 m and $N_{\mathrm{MAG}} = 2.7$. With the values of N not being an integer, these depths are expected to determine an intermediate point between the top and the centre.

The inversions (Fig. 10) were thus carried out by employing a positivity constraint, the horizontal constraints located by the boundary analysis and an average *structural index* $N_{\mathrm{av.}} = 2.5$. We stopped the inversions when the normalized misfit decreased under the threshold of 1e−11.

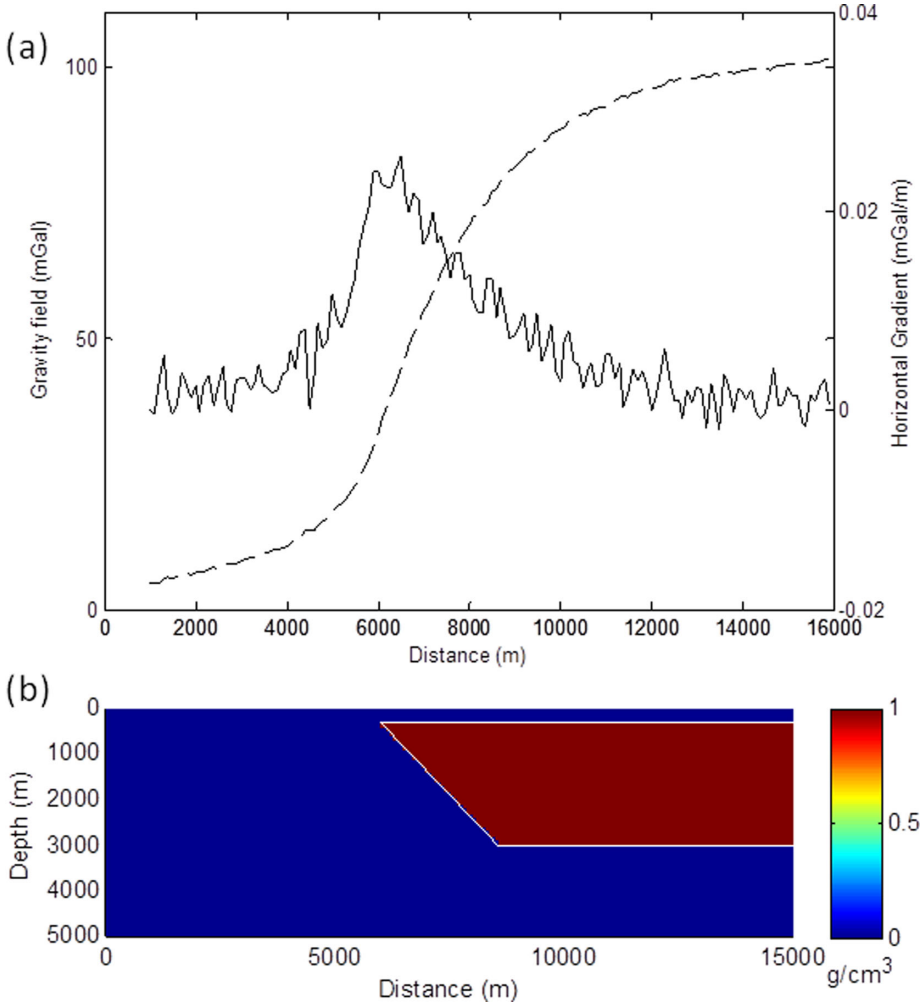

Figure 5. (a) Gravity anomaly generated by a dipping fault (45°) model with 1 g cm^{-3} density, 300 m depth-to-the-top and 2700 m thickness (dashed line) and modulus of the horizontal gradient of the gravity anomaly (solid line). Data are contaminated by a Gaussian noise with zero mean and standard deviation of 0.25 mGal. (b) Synthetic fault model.

Whereas the reconstruction obtained without any of the retrieved constraints, that is, the minimum-norm solution, lacks of any depth resolution (Fig. 10a), the solution constrained only by the depth-weighting function, with the exponent $\beta = N_{\text{av.}} = 2.5$ (Fig. 10b), shows a magnetization distribution located at the correct depth for the shallower source. However, the reconstructed position and magnetization of the deeper source is underestimated and both sources look blurred. The introduction of a further constraint about the horizontal position of the source edges as inferred by the EHD analysis significantly improved the reconstruction in terms of magnetization distribution for both sources (Fig. 10c). A further improvement to the reconstruction of the deeper source may be achieved by using as exponent of the depth-weighting function the exact structural index found by the data analysis for this source, that is, $N = 2.7$ (see Fig. 10d).

4 REAL DATA EXAMPLE

As an application of our inversion procedure to a real case, we carefully digitized the gravity data reported in Stavrev & Reid (2010) collected along a profile over the Venelin–Aksakov fault, which is located in the western bound of the Dolna Kamchia west–east trending depression, Eastern Bulgaria (Figs 11a and b). Geological and gravity data suggest the existence of a steep contact structure trending north–south between low-density Tertiary/Upper Cretaceous layers and the denser lower Cretaceous and deeper sediment layers. Core samples show a density contrast between the two complexes of 0.23 g cm^{-3}. The depth to the lower Cretaceous surface was found to be about 100 m in western part of the analysed profile (drillholes W-3 and W-4, Fig. 11a) and greater than 1250–2000 m in south-eastern areas (drillholes W-66 and W-27). The interpretative results from the analysis by Stavrev & Reid (2010), selected by the authors on the basis of the geological information, showed: i) a depth of 195 m for the upper edge point of the fault structure at a location $x_0 = 5875$ m; ii) a depth to the lower edge point of the contact of 2690 m.

Following our inversion strategy, we first evaluated the fault parameters to be used as constraints from the analysis of its gravity field. The *Multiridge Geometric Method* (Fedi *et al.* 2009) was applied to the first-order vertical derivative of the gravity field at low altitudes and then to the gravity field at high altitudes to obtain

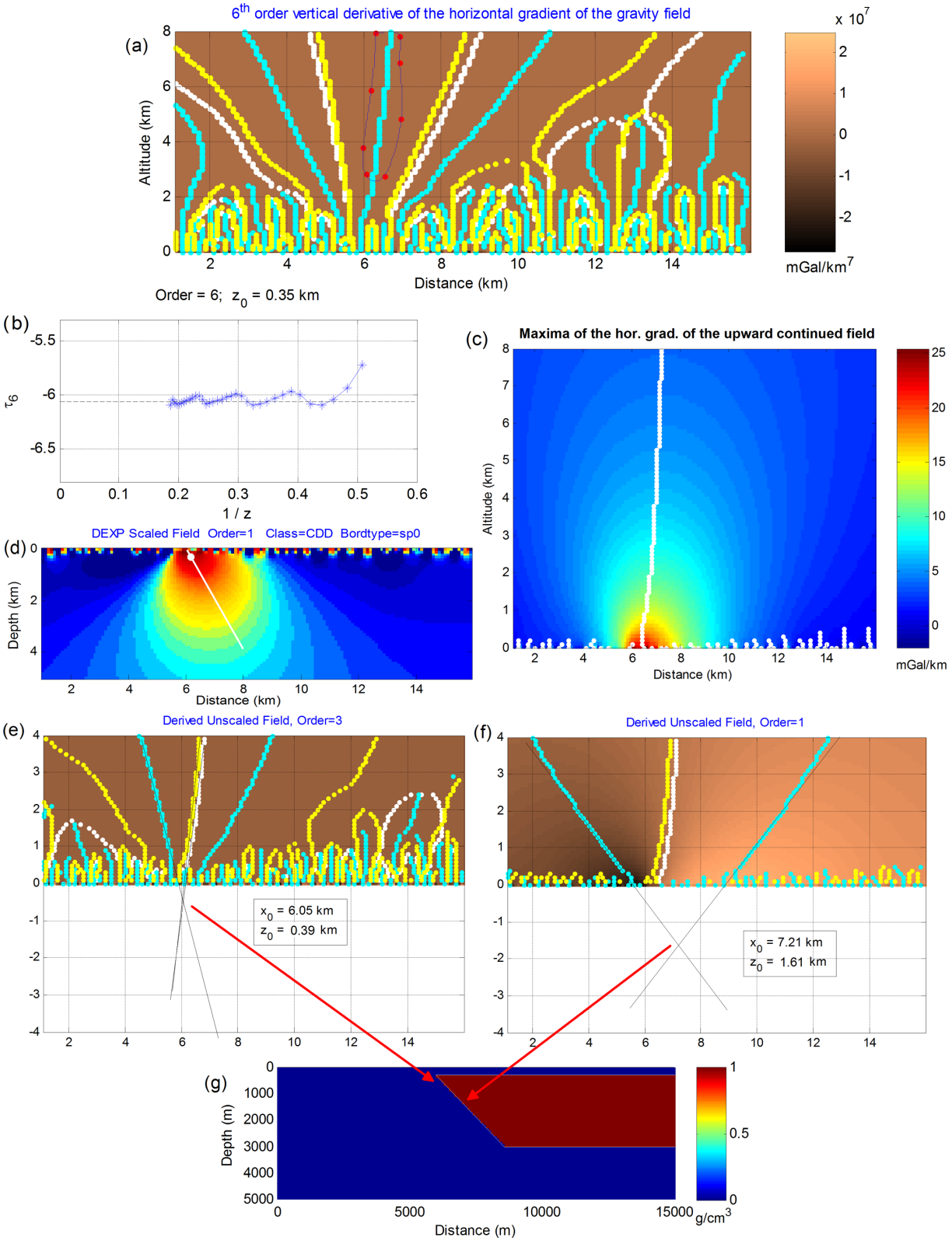

Figure 6. Analysis of the dipping fault data shown in Fig. 5(a). (a) and (b) Results of the *Scalfun Analysis* giving information about the source N and z_0. The intercept in (b) represents the value of $N +$ the differentiation order (sixth in this case). (c) Plot of maxima of the horizontal gradient of the upward continued field showing that the fault is dipping towards East. (d) *DEXP* analysis yielding information about the source z_0 and dip (shown by the maxima located at the shallowest depths). (e) and (f) *Multiridge Geometric method* applied to the third- (e) and first-order (f) vertical derivatives to obtain an estimation of the dip of the sloping boundary (g).

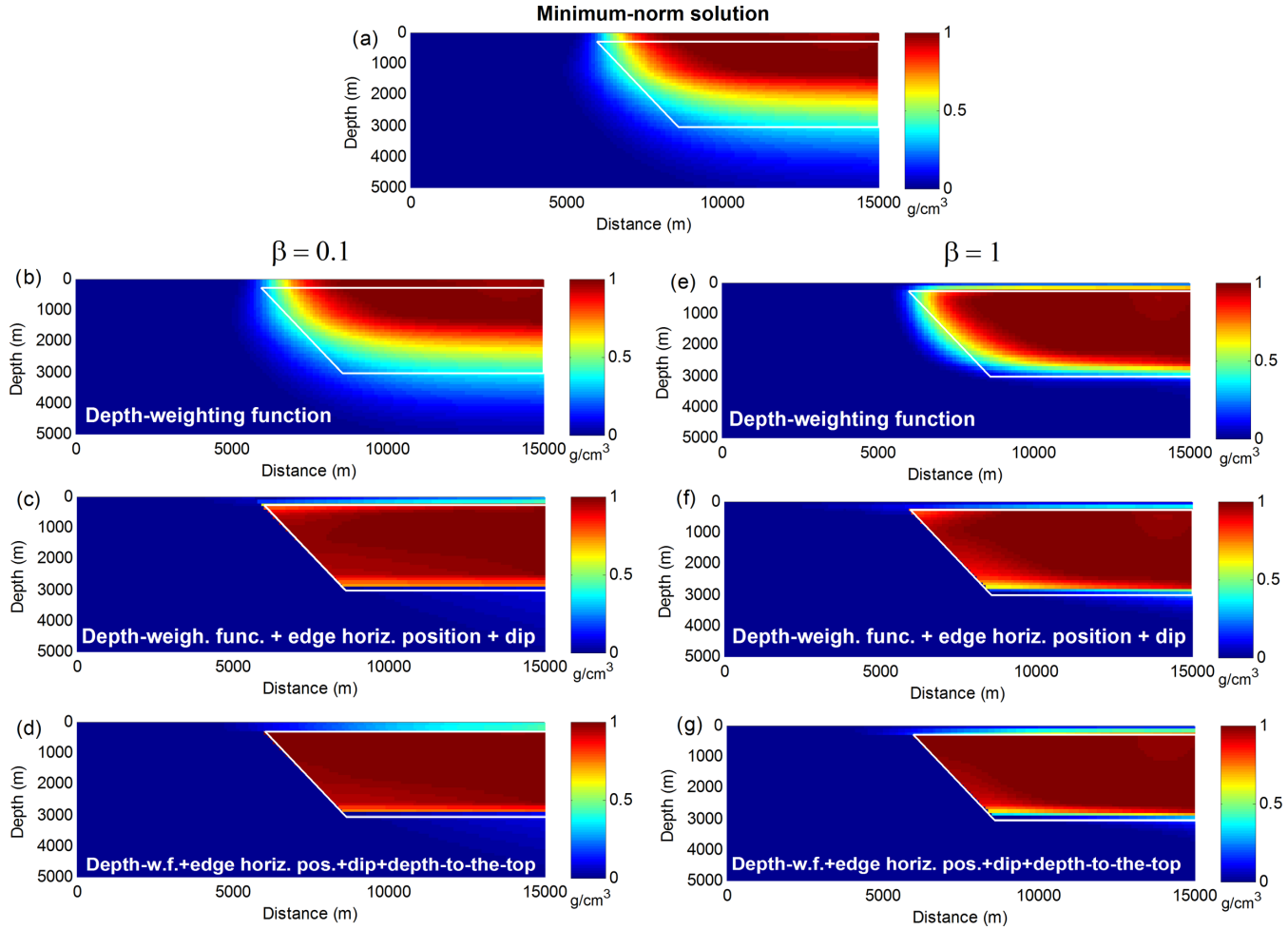

Figure 7. Density models obtained from the inversion of the dipping fault data contaminated by noise shown in Fig. 5(a) by resorting to different self-constraints: (a) reconstruction obtained without any constraint. (b) Density solution constrained by using a depth-weighting function with $\beta = N = 0.1$ retrieved from the data analysis (see Fig. 6b). (c) Solution with the additional constraint coming from the edge horizontal location and from the dip evaluation (see Fig. 5a and Figs 6e and f). (d) Solution with a further constraint on the location of the source depth-to-the-top (see Fig. 6b). (e)–(g) Same as plots as (b)–(d) but with $\beta = N = 1$, which allows obtaining a density distribution more balanced around the structure midpoint. In all the panels, the lines outline the actual source position. We note that the presence of noise in the data did not affect the quality of the solutions.

estimates, respectively, of the position of the upper (Fig. 12a) and lower part (Fig. 12b) of the dipping contact. This resulted in a contact depth-to-the-top slightly greater than 320 m and in a dip of about 76°. The subvertical characteristics of the fault were confirmed by the application of the McGrath's method (1991), which showed that the contact is slightly dipping towards the SE (Fig. 12d). We estimated the structural index of the structure by an indirect method that is selecting the scaling exponent of the *DEXP transformation* (Fedi 2007) such as the *DEXP* section gives a depth slightly greater than 300 m for the upper part of the dipping contact, consistently with the *Geometric Method*. The structural index so resulting was $N_{\mathrm{MAG}} = 0.1$ (Fig. 12c) and this value, very similar to the theoretical structural index of a contact, implies that the depth of about 320 m is relative to the top of the dipping fault.

For the 2-D data inversion, we used a data spacing of 125 m and discretized the source volume by 128 × 60 cubic cells, with 125 m sides. A positivity constraint was set for the inversions to avoid strong positive/negative density oscillations and to minimize the influence of regional gravity trends. The inversions were stopped when the normalized misfit decreased under the threshold of 1e−05.

The reconstructions obtained by resorting to the information derived from the data analysis of Fig. 12 as inversion constraints are shown in Fig. 13. The solution obtained by using only the structural index $N_{\mathrm{MAG}} = 0.1$ as depth-weighting function is characterized by a density maximum located at about 250 m depth (Fig. 13a), which is close to the depth-to-the-top resulting by *Multiridge Geometric Method* (slightly greater than 300 m), but the reconstruction does not image the shape of the dipping contact. The inclusion of constraints about the depth-to-the-top (set up in our case at a slightly deeper position than 320 m, that is, at 375 m, equal to the thickness of three cubic cells) and dip of the structure as inferred by the *Multiridge Geometric Method* (Figs 12a and b), and about the horizontal position of the of the fault ($x_0 = 5875$ m) as shown by the

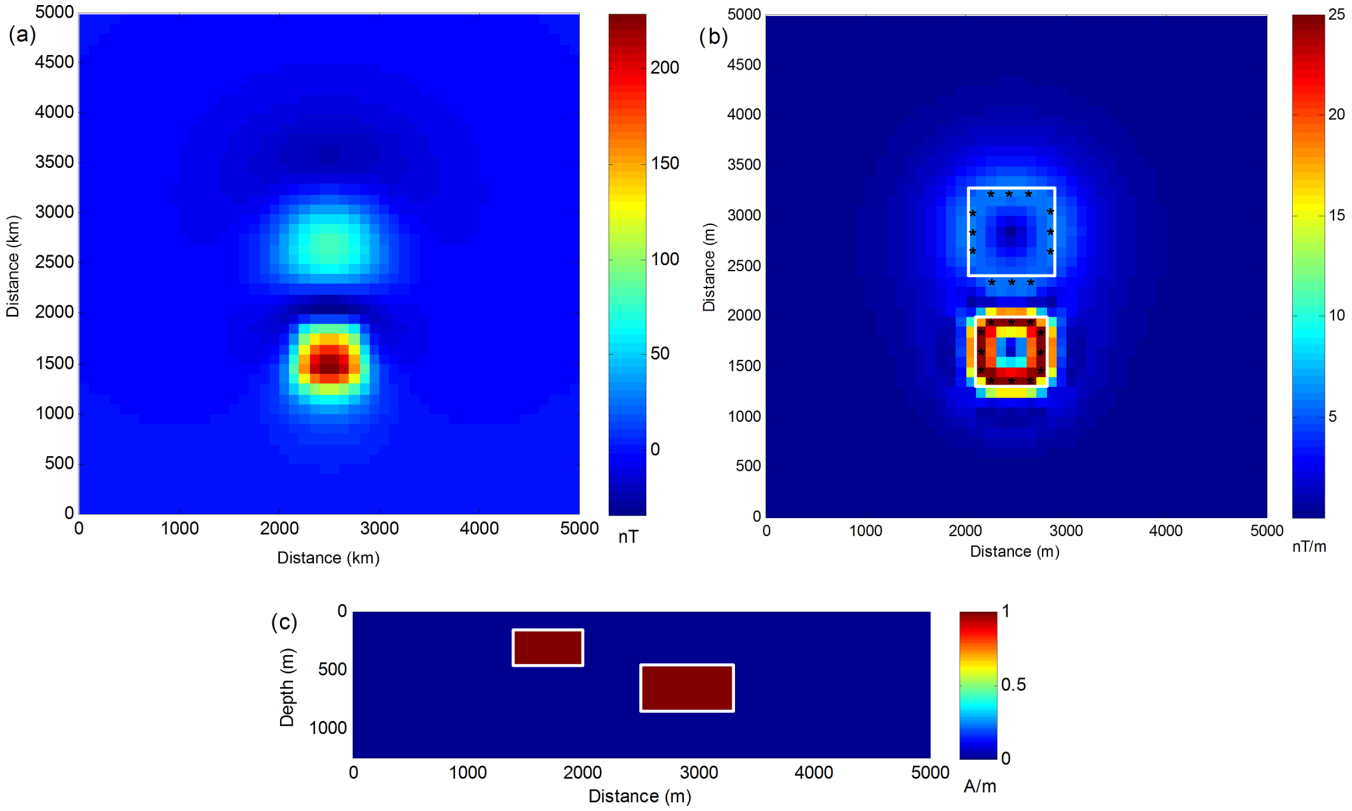

Figure 8. (a) Total field generated by two 3-D magnetized prismatic sources with contrast of 1 A m^{-1}. See text for details. (b) *Enhanced Horizontal Derivative* signal of the reduced to the pole data, whose maxima outline the source edge position. Stars show the location of the EHD maxima, and boxes show the actual sources' positions. (c) S-N vertical section of the synthetic model at $x = 2500$ m.

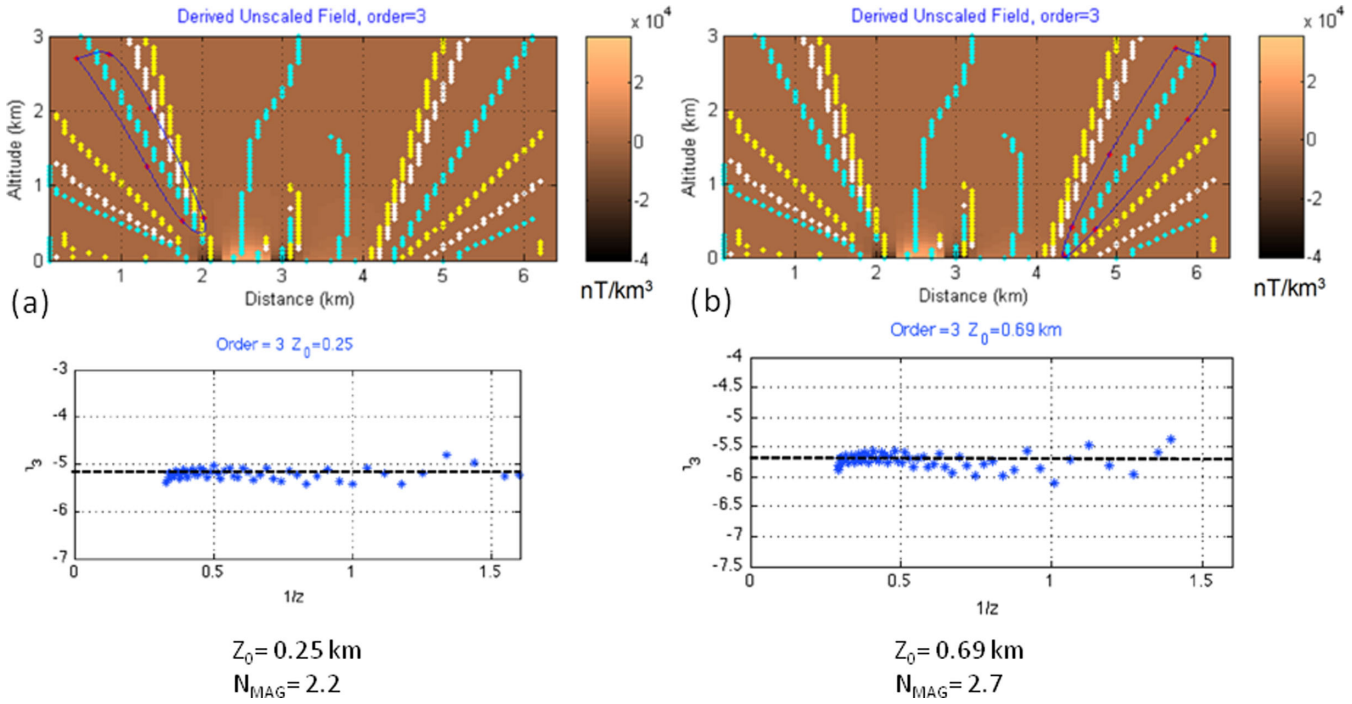

Figure 9. *Scaling Function analysis* carried out on the reduced to the pole data of Fig. 8(a). A ridge for each anomaly was selected from the vertical section of the third-order vertical derivative of the field (a) and (*b*). The plots of the rescaled scaling function by using the depths of 0.25 km (shallow source) and 0.69 km (deep source) versus the inverse of altitude are linear and the intercept represents the value of N_{MAG} + the differentiation order (third in this case) (Florio *et al.* 2009).

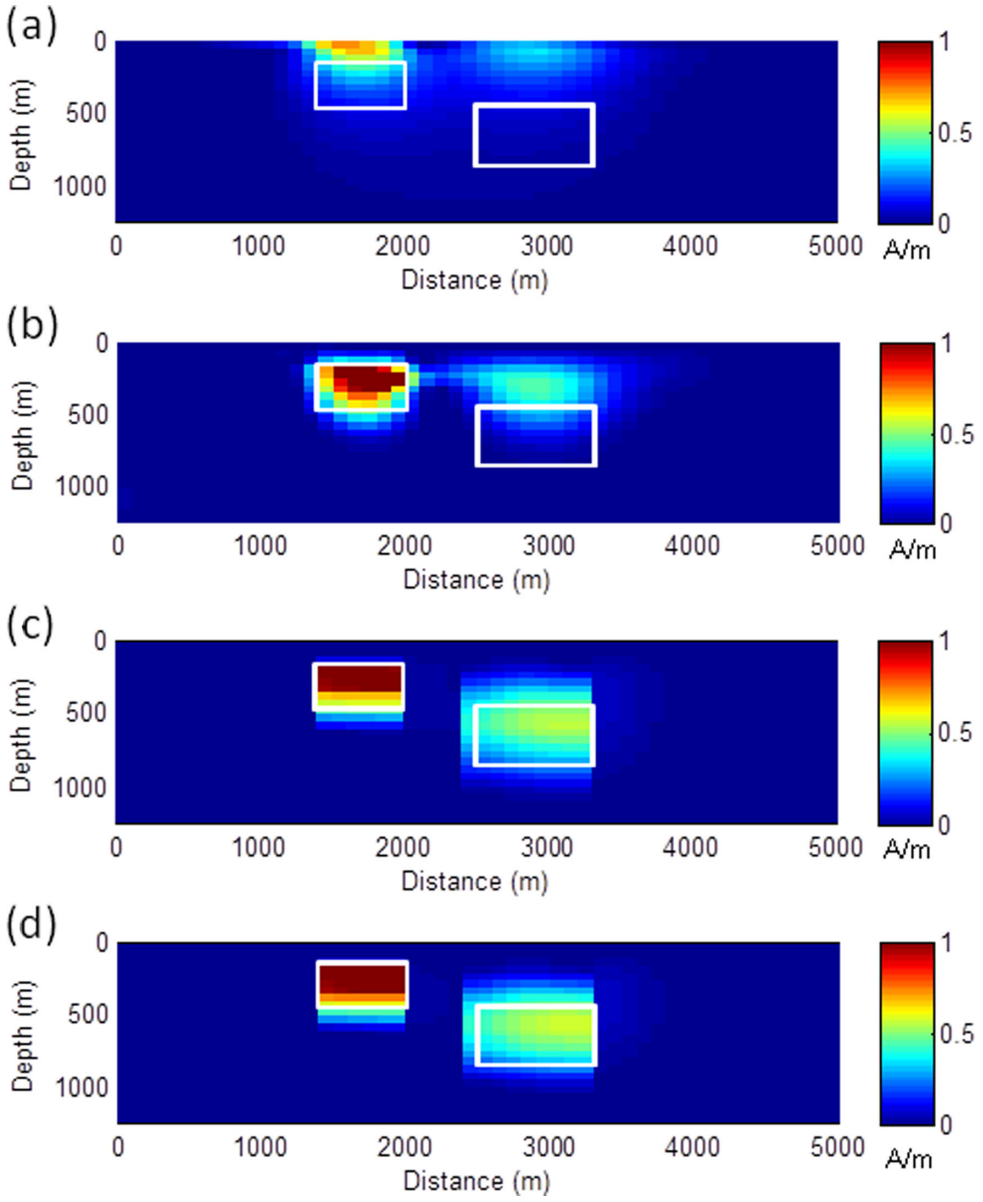

Figure 10. Vertical sections of the magnetization models obtained inverting the data in Fig. 8(a). (a) Minimum-norm solution. (b) Reconstruction obtained by using a depth-weighting function with an average exponent $\beta = N_{\text{av.}} = 2.5$. The reconstructed position and magnetization of the deeper source is underestimated and both sources look blurred. (c) Solution obtained with the additional constraint deriving from the EHD analysis: the magnetization distribution clearly shows information about the shallower source depth, edges and magnetization contrast. The deeper source position is well detected but its magnetization is underestimated. (d) The use of the exact structural index found for the deeper source, that is, $N = 2.7$, as exponent of the depth-weighting function allows an improvement in the reconstruction of the magnetization value for the deeper source. Boxes show the actual sources' positions.

horizontal gradient (Fig. 11b) lead to a solution that images the fault pattern rather well (Fig. 13b). It is characterized by a density distribution that agrees with the geological information and the results of the analysis by Stavrev & Reid (2010). More specifically, the solution shows a dense subvertical contact structure trending north–south whose density contrast with less dense layers is close to the density contrast determined by core samples (0.23 g cm^{-3}). This structure has a depth range of about 300–2700 m (Fig. 13b), which is close to the depth, ranging from 195 to 2690 m, retrieved by Stavrev & Reid (2010) and to the depth to the lower Cretaceous surface found in drillholes W-3 and W-4 (about 100 m) and in drillholes W-66 and W-27 (about 1250–2000 m).

5 CONCLUSIONS

A priori information is needed to solve inverse problems for potential fields. This is because of the general ambiguity characterizing such problems. In this paper, we distinguished between external (drill logs, geological/geophysical information) and field-based constraints, such as depth, structural index, horizontal position and

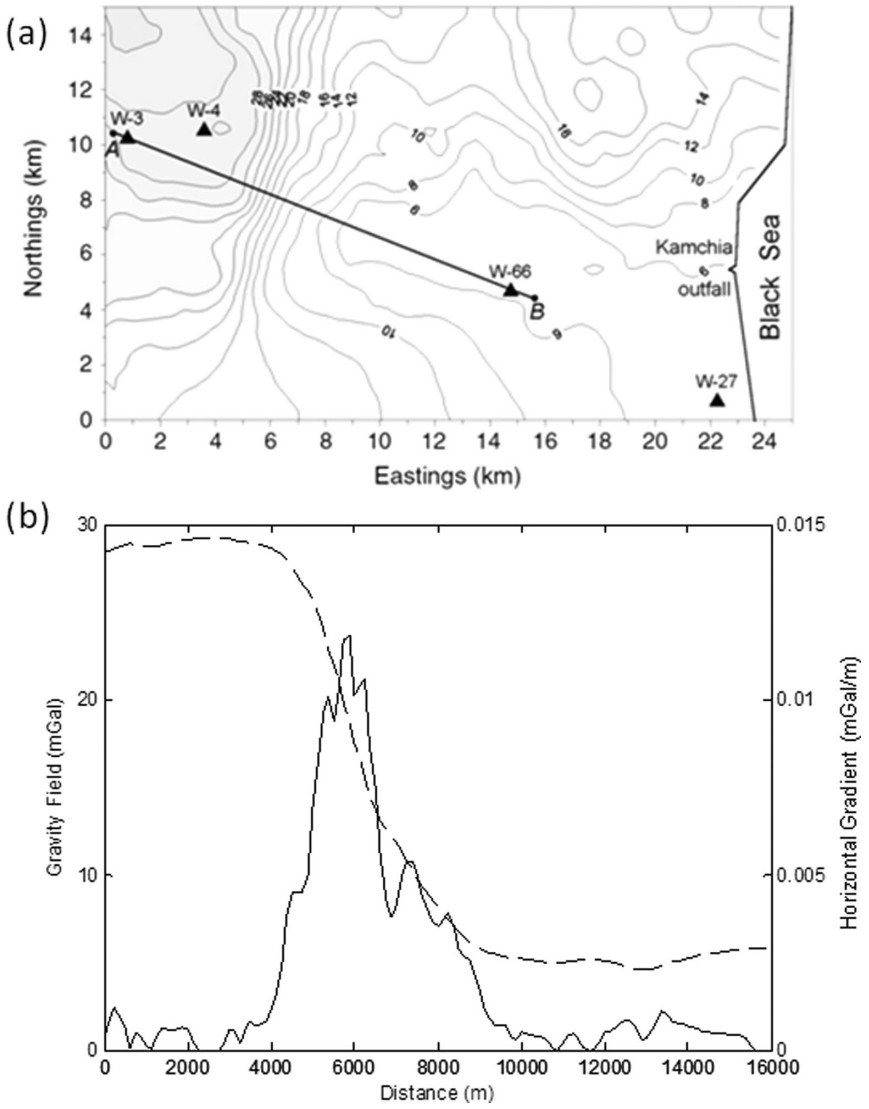

Figure 11. The real case of the Venelin–Aksakov fault, Bulgaria. (a) Gravity map collected in the study area (from Stavrev & Reid 2010). (b) Gravity data along the profile shown in (a) (dashed line) and modulus of the horizontal gradient of the gravity anomaly (solid line).

dip of the source edges. We presented a self-constrained inversion procedure based only on the intrinsic properties of the potential field anomaly, which makes use of constraints such as depth, structural index, horizontal position and dip of the source edges. The procedure applies to underdetermined problems and involves scenarios where the source distribution can be assumed to be of a simple character.

We showed that despite a few known assumptions/limitations connected to the boundary analysis and despite some possible error in the estimation of source parameters, adding as inversion constraints information retrieved by a previous analysis of the data has a great potential to lead to well-constrained solutions with respect to the source depth and to the horizontal variations of the source-density distribution. The employed constraints can be successfully retrieved by the many methods available in the toolbox of the potential field interpreter. We concentrated our research on the use of multiscale methods that are particularly suitable for a detailed analysis of potential fields. Our analysis of synthetic data, with or without added noise, and on real data, demonstrated that the more self-constraints are included in the inversion, the less important is the role of the tuning of the depth-weighting function through the actual value of the source structural index. Although here we dealt with of 2-D gravity and 3-D magnetic data, our procedure is also suited to the analysis of potential field gradients. The success of our strategy suggests that potential fields have a great potential to yield realistic source distributions even without supplying other information of external origin, at least when relatively simple property distributions are implied.

ACKNOWLEDGEMENTS

We are very grateful to Peter Lelièvre, to an anonymous reviewer and to the Editor Dr. Richard Holme, for their thorough reviews. The manuscript benefited from Per Christian Hansen's comments and Bill McGann's language revision.

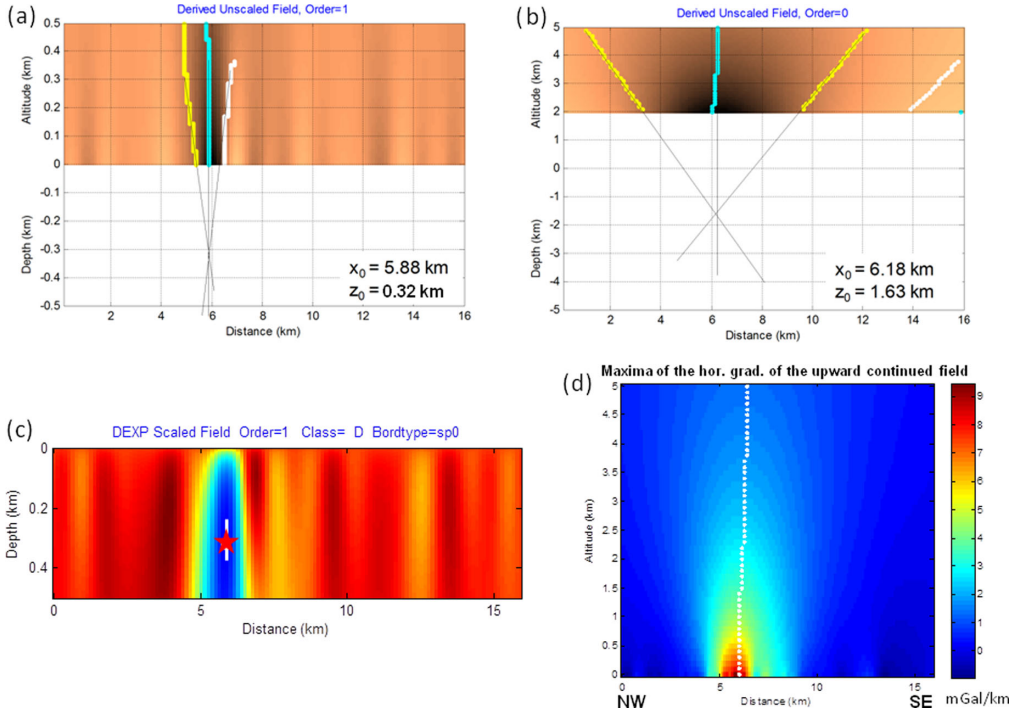

Figure 12. Analysis of the data shown in Fig. 11(b). (a) and (b) Results of the *Multiridge Geometric method* applied to the first-order vertical derivative of the gravity field at low altitudes and to the gravity field at high altitudes to obtain estimates of the position, respectively, of the upper and lower part of the contact and thus of its dip. (c) *DEXP* analysis yielding information about the source structural index *N*. (d) Plot of maxima of the horizontal gradient of the upward continued field showing that the fault is slightly dipping towards SE.

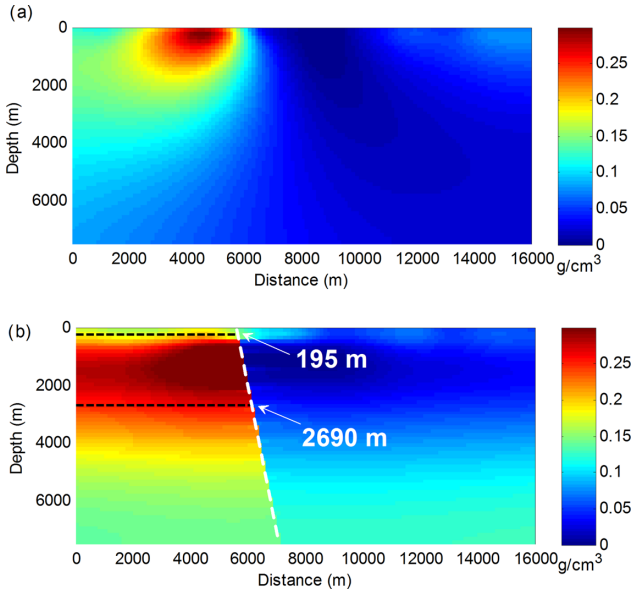

Figure 13. Density models obtained from the inversion of the real gravity data shown in Fig. 11(b). (a) Reconstruction constrained by a depth-weighting function with $\beta = N = 0.1$ retrieved from the data analysis (see Fig. 12). The source top is reconstructed at its correct depth but the shape of the dipping contact is not well imaged and the horizontal position of the density maximum does not coincide with the estimates shown in Fig. 12. (b) Solution obtained with additional constraints about the fault upper edge depth-to-the-top, horizontal position and about the fault dip. The reconstructed density distribution is in agreement with the results of the analysis by Stavrev & Reid (2010); the horizontal dashed lines in (b) represent the estimates of the depths to the fault's top and bottom as found by Stavrev & Reid (2010).

REFERENCES

Al-Chalabi, M., 1971. Some studies relating to nonuniqueness in gravity and magnetic inverse problems, *Geophysics,* **36,** 835–855.

Ash, M.R., Wheeler, M., Miller, H., Farquharson, C.G. & Dyck, A.V., 2006. Constrained three-dimensional inversion of potential field data from the Voisey's Bay Ni-Cu-Co deposit, Labrador, Canada, in *Proceedings of the 76th Annual Meeting of the Society of Exploration Geophysicists,* New Orleans, 1–6 October, 2006, pp. 1333–1337.

Barbosa, V.C.F., Silva, J.B.C. & Medeiros, W.E., 1999. Stability analysis and improvement of structural index estimation in Euler deconvolution, *Geophysics,* **64**(1), 48–60.

Barnes, G. & Barraud, J., 2012. Imaging geologic surfaces by inverting gravity gradient data with depth horizons, *Geophysics,* **77,** G1–G11.

Boulanger, O. & Chouteau, M., 2001. Constraints in 3D gravity inversion, *Geophys. Prospect.,* **49,** 265–280.

Bruno, P.P., de Alteriis, G. & Florio, G., 2002. The western undersea section of the Ischia volcanic complex (Italy, Tyrrhenian sea) inferred by marine geophysical data, *Geophys. Res. Lett.,* **29**(9), 57-1–57-4.

Chasseriau, P. & Chouteau, M., 2003. 3D gravity inversion using a model of parameter covariance, *J. appl. Geophys.,* **52,** 59–74.

Cella, F. & Fedi, M., 2012. Inversion of potential field data using the structural index as weighting function rate decay, *Geophys. Prospect.,* **60,** 313–336.

Cella, F., Fedi, M. & Florio, G., 2009. Toward a full multiscale approach to interpret potential fields, *Geophys. Prospect.,* **57,** 543–557.

Cooper, G.R.J. & Cowan, D.R., 2006. Enhancing potential field data using filters based on the local phase, *Comput. Geosci.,* **32,** 1585–1591.

Corbato, C.E., 1965. A least-squares procedure for gravity interpretation, *Geophysics,* **30,** 228–233.

Cordell, L.E. & Grauch, V.J.S., 1985. Mapping basement magnetization zones from aeromagnetic data in the San Juan Basin, New Mexico, in *The Utility of Regional Gravity and Magnetic Anomaly Maps,* pp. 181–197, ed. Hinze, W.J., Society of Exploration Geophysicists.

Cordell, L.E. & Henderson, R.G., 1968. Iterative three-dimensional solution of gravity anomaly data using a digital computer, *Geophysics,* **33,** 596–601.

Engl, H.W., Hanke, M. & Neubauer, A., 1996. *Regularization of Inverse Problems*, Kluwer Academic Publishers, 321 pp.

Farquharson, C.G., Ash, M.R. & Miller, H., 2008. Geologically constrained gravity inversion for the Voisey's Bay ovoid deposit, *Leading Edge,* **27,** 64–69.

Fedi, M, 2002. Multiscale derivative analysis a new tool to enhance detection of gravity source boundaries at various scales, *Geophys. Res. Lett.,* **29**(2), 16-1–16-4.

Fedi, M., 2007. DEXP: a fast method to determine the depth and the structural index of potential field sources, *Geophysics,* **72,** 1–11.

Fedi, M. & Florio, G., 2001. Detection of potential fields source boundaries by enhanced horizontal derivative method, *Geophys. Prospect.,* **49,** 40–58.

Fedi, M., Florio, G. & Quarta, T., 2009. Multiridge analysis of potential fields: geometrical method and reduced Euler deconvolution, *Geophysics,* **74,** L53–L65.

Fedi, M., Hansen, P.C. & Paoletti, V., 2005. Tutorial: analysis of depth resolution in potential-field inversion, *Geophysics,* **70,** A1–A11.

Fedi, M. & Pilkington, M., 2012. Understanding imaging methods for potential field data, *Geophysics,* **77,** G13–G24.

Fedi, M., Florio, G. & Paoletti, V., 2012. Local homogeneity of potential fields and fractional homogeneous functions: a new theory for improved source parameter estimation, in *Proceedings of the 82nd Annual Meeting of the Society of Exploration Geophysicists,* Las Vegas, 4–9 November, 2012, pp. 1–5.

Florio, G. & Fedi, M., 2006. Euler deconvolution of vertical profiles of potential field data, *SEG Technical Program Expanded Abstracts,* 76th SEG Annual Meeting, New Orleans, 1–6 October, 2006, pp. 958–962.

Florio, G., Fedi, M. & Rapolla, A., 2009. Interpretation of regional aeromagnetic data by the scaling function method: the case of Southern Apennines (Italy), *Geophys. Prospect.,* **57**(4), 479–489.

Florio, G. & Fedi, M., 2013. Multiridge Euler deconvolution, *Geophys. Prospect.,* in press, doi:10.1111/1365-2478.12078.

Grauch, V.J.S. & Cordell, L., 1987. Limitations of determining density or magnetic boundaries from the horizontal gradient of gravity or pseudo-gravity data, *Geophysics,* **52,** 118–121.

Guillen, A., Calcagno, Ph., Courrioux, G., Joly, A. & Ledru, P., 2008. Geological modelling from field data and geological knowledge. Part II. Modelling validation using gravity and magnetic data inversion, *Phys. Earth planet. Int.,* **171,** 158–169.

Hansen, P.C., 1998. *Rank-Deficient and Discrete Ill-Posed Problems: Numerical Aspects of linear Inversion*, Society of Industrial and Applied Mathematics, 247 pp.

Last, B.J. & Kubik, K., 1983. Compact gravity inversion, *Geophysics,* **48,** 713–721.

Lelièvre, P.G. & Oldenburg, D.W., 2009. A comprehensive study of including structural orientation information in geophysical inversions, *Geophys. J. Int.,* **178,** 623–637.

Li, Y. & Oldenburg, D.W., 1996. 3-D inversion of magnetic data, *Geophysics,* **61,** 394–408.

Li, Y. & Oldenburg, D.W., 1998. 3-D inversion of gravity data, *Geophysics,* **63,** 109–119.

McGrath, P.H., 1991. Dip and depth extent of density boundaries using horizontal derivatives of upward-continued gravity data, *Geophysics,* **56,** 1533–1542.

McGrath, P.H. & Hood, P.J., 1973. An automatic least-squares multimodel method for magnetic interpretation, *Geophysics,* **38,** 349–358.

Miller, H.G. & Singh, V., 1994. Potential field tilt—a new concept for location of potential field sources, *J. appl. Geophys.,* **32,** 213–217.

Moreau, F., Gibert, D., Holschneider, M. & Saracco, G., 1999. Identification of sources of potential fields with the continuous wavelet transform: basic theory, *J. geophys. Res.,* **104**(B3), 5003–5013.

Nabighian, M.N. & Hansen, R.O., 2001. Unification of Euler and Werner deconvolution in three dimensions via the generalized Hilbert transform, *Geophysics,* **66,** 1805–1810.

Paoletti, V., 2012. Remarks on Factors influencing Shear Wave Velocities and their role in evaluating Susceptibilities to Earthquake-triggered Slope Instability: case study for the Campania area (Italy), *Nat. Hazards Earth Syst. Sci.,* **12,** 2147–2158.

Paoletti, V., D'Antonio, M. & Rapolla, A., 2013. The Structural Setting of the Ischia Island within the Neapolitan Volcanic Area: Inferences from Geophysics and Geochemistry, *J. Volcanol. Geotherm. Res.,* **249,** 155–173.

Paoletti, V., Fedi, M., Florio, G. & Rapolla, A., 2007. Localized cultural de-noising of high-resolution aeromagnetic data, *Geophys. Prospect.,* **55,** 412–432.

Pedersen, L.B., 1977. Interpretation of potential field data—a generalized inverse approach, *Geophys. Prospect.,* **25,** 199–230.

Pilkington, M., 2009. 3D magnetic data-space inversion with sparseness constraints, *Geophysics,* **74,** L7–L15.

Portniaguine, O. & Zhdanov, M.S., 2002. 3-D magnetic inversion with data compression and image focusing, *Geophysics,* **67,** 1532–1541.

Rapolla, A., Di Nocera, S., Matano, F., Paoletti, V. & Tarallo, D., 2012. Regional zonation on seismic-induced landslide susceptibility: application of a new procedure to Campania, Southern Italy, *Nat. Hazards,* **61,** 115–126.

Sailhac, P., Galdeano, A., Gibert, D., Moreau, F. & Delor, C., 2000. Identification of sources of potential fields with the continuous wavelet transform: complex wavelets and application to aeromagnetic profiles in French Guiana, *J. geophys. Res.,* **105**(B8), 19 455–19 475.

Secomandi, M., D'Amico, S., Paoletti, V. & Rapolla, A., 2013. Macroseismic Attenuation in the Campanian Area, Southern Italy, *Izvestiya, Phys. Sol. Earth,* **49**(3), 416–425.

Shamsipour, P., Marcotte, D. & Chouteau, M., 2012. Integrating multiscale parameters information into 3D stochastic magnetic anomaly inversion, *Geophysics,* **77,** D85–D93.

Silva, J.B.C. & Barbosa, V., 2004. Generalized radial inversion of 2D potential field data, *Geophysics,* **69,** 1405–1413.

Silva, J.B.C. & Barbosa, V.C.F., 2006. Interactive gravity inversion, *Geophysics,* **71,** J1–J9.

Silva, J.B.C., Medeiros, W. & Barbosa, V., 2001. Potential-field inversion: choosing the appropriate technique to solve a geologic problem, *Geophysics,* **66,** 511–520.

Stavrev, P. & Reid, A., 2010. Euler deconvolution of gravity anomalies from thick contact/fault structures with extended negative structural index, *Geophysics,* **75,** I51–I58.

Verduzco, B., Fairhead, J.D. & Green, C.M., 2004. New insights into magnetic derivatives for structural mapping, *Leading Edge,* **23,** 116–119.

Whitehill, D.E., 1973. Automated interpretation of magnetic anomalies using the vertical prism model, *Geophysics,* **38,** 1070–1087.

Wijns, C. & Kowalczyk, P., 2007. Interactive geophysical inversion using qualitative geological constraints, *Exploration Geophys.,* **38,** 208–212.

Wijns, C., Perez, C. & Kowalczyk, P., 2005. Theta map: edge detection in magnetic data, *Geophysics,* **70,** 39–43.

Williams, N., Lelièvre, P.G. & Oldenburg, D.W., 2009. Constraining gravity and magnetics inversions for mineral exploration using limited geological data, in *Proceedings of the 20th ASEG Conference,* Adelaide, 22–25 February 2009.